VOL. 12, NO. 4, FEBRUARY 2017 ISSN 1819-6608
ARPN Journal of Engineering and Applied Sciences

www.arpnjournals.com

NONLINEAR CONTROL FOR GRID CONNECTED WIND ENERGY SYSTEM WITH MULTILEVEL INVERTER

Hamid Ouadi[1], Adil Barra[1] and Khalid El Majdoub[2]
[1]PMMAT Lab, University Hassan II, Faculty of Science, Casablanca, Morocco
[2]PAM Lab, University Hassan II, Faculty of Science, and Technology, Mohammedia, Morocco
E-Mail: hamidouadi3@yahoo.fr

ABSTRACT

This paper deals with the problem of interfacing a wind turbine generator with an electrical three phase grid in the presence of nonlinear loads. Wind systems are generally connected to the grid through an AC/DC inverter in the generator side, followed by a DC/AC converter in the grid side. In this work, the considered DC/AC converter is based on multilevel neutral point clamped topology, and will operates simultaneously as an interfacing system and as an active power filter. The control objective is threefold: *(i)* transferring the extracted active power from the wind turbine generator to the power grid; *(ii)* cancelling harmonic currents and reactive power absorbed by the nonlinear load; *(iii)* balancing capacitor voltages and regulating the DC link voltage. The first and second control aims will be achieved using the backstepping design technique. The third objective dealing with the DC link voltage regulator will be achieved with a sliding mode technical design. The performances of the proposed control system are formally analyzed using tools from Lyapunov's stability. Simulations show that the proposed controller achieved the listed objectives under widely varying load and wind speed profiles.

Keywords: DFIG Generator, 3-Level NPC inverter, generalized average modeling, shunt active power filter, p-q theory.

1. INTRODUCTION

Wind energy has become one of the most important sources of renewable energy [1]. Nowadays with the development of control tools, wind turbine systems are no longer limited to active power generators in distribution grids, but they also contribute in improving the quality of produced energy. In fact, supplementary requirements could be imposed to wind system such as: the compensation of reactive load power, the cancellation of harmonic load currents and the improvement of the voltage quality at the Point of Common Coupling (PCC).

The considered wind system is described in Figure-1. It is constituted by a wind turbine associated to a doubly fed induction generator (DFIG). The DFIG stator is being directly connected to the grid while the rotor is linked through an AC-DC inverter followed by a DC-AC. The main advantage of this topology is that the static converters are dimensioned just to endure a portion of the nominal DFIG power (practically 30%) [2]. consequently this structure of wind system offers low costs and high robustness. The inverter placed on the rotor side is generally commanded in such a way to ensure a variable speed operation mode of the wind turbine. This allows a maximum power point tracking (MPPT objective). The grid side converter (GSC) ensures the control of the energy exchanged between the DFIG and the distribution network. Moreover, this second converter can also meet the requirements of standards quality imposed to the produced electricity. Indeed, in addition to the control of the extracted power, this converter can be used whether to perform filtering functions of the current / voltage harmonics, to compensate the reactive power or to regulate network frequency.

The control of the rotor side converter (ensuring the MPPT objective) has been widely discussed in the literature [3, 4]. In this paper, we focus only on the DC-AC converter placed on the electrical grid side. As presented in Figure-2, the considered converter in this paper is a multi-level. Compared with the conventional structure with two levels, the three-level topology generates AC currents and voltages having a lower harmonic distortion. This is ensured by the high number of voltage levels provided by the multi-level structure [5]. In addition, for a given power, the constraints on the multilevel inverter power switches are less hard than in the case of a two level inverter. Therefore, for high power applications, the cost of the multilevel inverter is much lower. In addition, this inverter can also reduce abrupt variations in the AC output voltage. This will avoid some problems of electromagnetic compatibility.

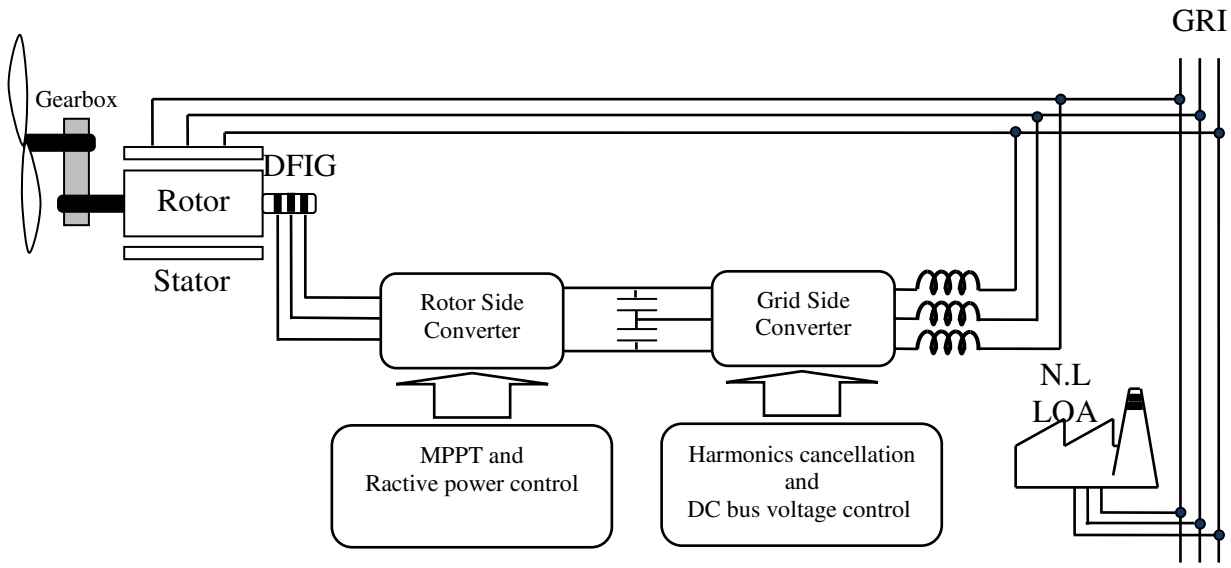

Figure-1. General scheme of the considered wind system.

Among the multi-level configurations, the more famous and reliable are: The H bridge converter, the flying capacitors topology and the Neutral Point Clamped topology. The multi-level Neutral Point Diode Clamped (NPC) converter has been widely used for applications in high power drives and utility systems [6]–[8]. As compared with the other prevalent multi-level converter topologies [9], the NPC converter uses a fewer number of capacitors and switches per phase to synthesize the desired output voltage levels. It is, therefore, more economical and reliable. This paper is concerned with the three-level NPC converter control.

Furthermore, various multilevel Pulse Width Modulation (PWM) techniques are proposed to generate gate signals for the NPC inverters [10]. Indeed, for the AC voltage control behavior, one distinguishes two main variants of the pulse width modulation (PWM) generator: Sinusoidal PWM (SPWM) (also called Carrier Based PWM) and Space Vector PWM (SVPWM). The SVPWM is very popular in NPC applications due to its harmonic reduction opportunities and neutral point balance [10]. However, this technique has a relatively large computation time and its algorithms are more complex in control implementation [11]. Furthermore, SPWM technique provides a good compromise between simplicity of implementation, harmonic generation and low switching losses [10]. For these reasons the SPWM technique has been retained in this work (see Figure-4).

Moreover, to ensure a proper connection of the wind system to the grid, some constraints must be taken into account at the NPC control design. In fact, the main technical challenge in any application of the NPC inverter is to maintain the two capacitor voltages equal and at a pre-specified level (see Figure-2). These voltages can either rapidly and drastically diverge during transients or slowly drift during normal operations due to the wind system imperfections. The principal motivation behind keeping the balance of the capacitor voltages is to maintain the harmonic distortion of the terminal voltage at minimum. Indeed, the bridge capacitor unbalancing causes a neutral point fluctuation problem. It is increasing the voltage stresses on the semiconductor devices, introduces harmonics and distorts the waveform of the output voltage which results in an increase in the total harmonic distortion (THD).

The inverte control problem for wind energy systems has been addressed using many control techniques that can be classified into three categories: The first one includes methods using hysteresis operators or fuzzy logics [12, 13]. These methods do not make use of the exact nonlinear wind system model in the control design. Consequently, the obtained controllers are generally not backed up by formal stability analysis and their performances are only illustrated by simulations. The second category of methods is limited to linear controllers [14]. As a matter of fact, optimal performances are not guaranteed with linear techniques on a wide range variation of the operation point, due to the nonlinear nature of the controlled system. The third category of methods includes nonlinear controllers, designed on the basis of the system accurate nonlinear models [15]. However, the proposed nonlinear controllers were limited to the case of two-level topology converter. The problem is that for high power applications, connecting several units of production, the two levels structure is, on the one hand, more expensive than the three levels topology and, on the other hand, cannot ensure large quality performances of the energy produced.

In other previous works [16], the grid connection of wind energy system is ensured through a single converter (matrix converter). In fact, the authors of this paper tried to achieve the MPPT control objective and the DC bus control with a unique converter. The "perturb and observe" algorithm has been performed for extracting the optimal wind power. However, the required frequency switches, as well as the merger of the objectives on the

same converter reduce both the control flexibility and the switches lifetime.

To our knowledge, there is no work dealing with the nonlinear control of the multilevel NPC inverter ensuring the wind system Grid connection. Indeed, several papers have developed nonlinear controllers for the NPC inverter but limited to active filtering applications [17]. In [18] a robust nonlinear controller is proposed to compensate harmonics load currents. However, it is not designed to cancel the reactive power. Moreover, an auxiliary structure was proposed for the DC-link balancing problem. This leads to an increase in the inverter complexity, to additional energy losses and to the introduction of lower order harmonics at the inverter output voltage.

In this paper, a new controller is developed for the DC/AC inverter ensuring the grid connection of the considered wind energy system (see Figure-1). Recall that this inverter presents a three level NPC structure. In practice, to ensure proper operation of the wind system, it is necessary to ensure both the balance of the capacitor voltages and the regulation of the DC bus voltage to a defined level.

The required control objectives are as follow:

a) Ensuring the transit of the extracted optimal wind power to the grid.
b) Regulating the DC bus voltage.
c) Balancing the capacitive divider placed on the DC side of the inverter
d) Compensating the reactive power and the harmonics currents generated by nonlinear load.

The achievement of the last objective entails real-time construction of the reference signals from harmonic and reactive load currents. The involved nonlinear control laws are designed by the backstepping technique. The controller thus obtained is illustrated by Figure-3. It is multi-loop including DC voltage controller, DC balance voltage controller, and inverters' output currents controller. It is formally shown, using tools from Lyapunov's stability, that all control objectives are asymptotically achieved. The controller performances are further illustrated by numerical simulation considering a various wind profile with different nonlinear loads.

Table-1. System notations.

Notations	Description
L	Decoupling filter inductor
C	Compensator capacity
$\boldsymbol{R}$	Decoupling filter resistor
$\boldsymbol{V_{dc}}$	Inverter's DC voltage
$\boldsymbol{i_{pd}, i_{pq}}$	Inverter output current in d-q frame
$\boldsymbol{V_{c1}, V_{c2}}$	Capacitor's simple voltages
$\boldsymbol{V_{sd}, V_{sq}}$	Voltages at the Point of commune coupling in d-q frame
$\boldsymbol{V_{eff}}$	RMS network voltage
$\boldsymbol{W_{abc}}$	Switching functions
$\boldsymbol{a_0}$	The switching function's amplitude
$\boldsymbol{a_2, a_3}$	The DC voltage offsets
$\boldsymbol{a_1}$	phase angle of the modulating waveform
$\boldsymbol{I_{dc}}$	Current at the input of the inverter
$\boldsymbol{V_{dc\_ref}}$	Inverter's DC voltage reference
$\boldsymbol{i_{rd}, i_{rq}}$	d-q components of DFIG rotor current
$\boldsymbol{i_{Lh\_d}, i_{Lh\_q}}$	Harmonics currents in dq frame
$\boldsymbol{i_{pd}^*, i_{pq}^*}$	Inverter output current references in dq frame
$\boldsymbol{P_{Rotor}, P_{Stator}}$	Rotor and stator DFIG powers
$\boldsymbol{P_W}$	Available wind power
$\boldsymbol{P_{pcc}}$	Inverter output power.
$\boldsymbol{\bar{p}}$	Mean value of the instantaneous real power
$\boldsymbol{\tilde{p}}$	Harmonic component of the instantaneous real power
$\boldsymbol{\bar{q}}$	Mean value of the instantaneous imaginary power
$\boldsymbol{\tilde{q}}$	Harmonic component of the instantaneous imaginary power
$\boldsymbol{i_{rd}, i_{rq}}$	Rotor currents d-q components
$\boldsymbol{M_{sr}}$	DFIG Mutual cyclic induction
$\boldsymbol{R_s, R_r}$	DFIG Stator, Rotor resistance (per phase)
$\boldsymbol{i_{sd}, i_{sq}}$	Stator current (d-q) components
$\boldsymbol{V_{rd}, V_{rq}}$	Rotor voltage (d-q) components
$\boldsymbol{V_{td}, V_{tq}}$	AC NPC inverter voltages in d-q coordinates
$\boldsymbol{L_s, L_r}$	DFIG Stator, Rotor cyclic induction
$\boldsymbol{p}$	Poles pairs
$\boldsymbol{\omega_s}$	Stator pulsation
$\boldsymbol{f_s}$	Grid frequency
$\boldsymbol{\omega}$	Grid pulsation
$\boldsymbol{Re\{.\}}$	Real part of a complex number
$\boldsymbol{Im\{.\}}$	Imaginary part of a complex number

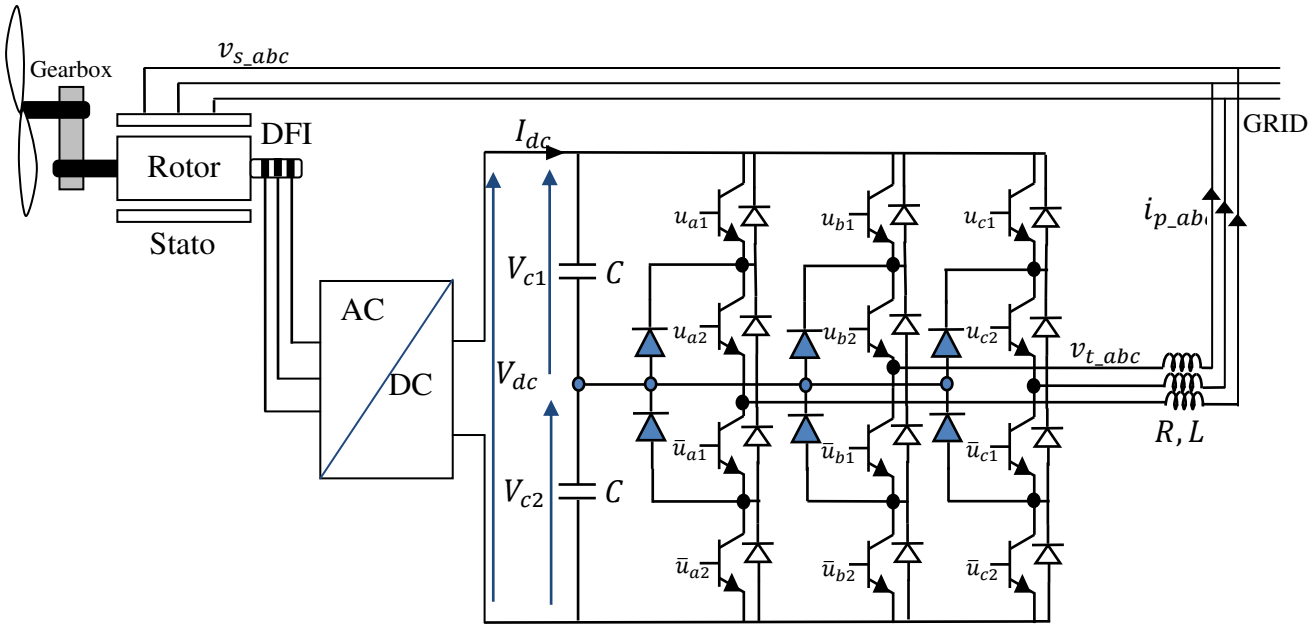

Figure-2. 3 level NPC converter structure.

In the light of the above description, it is evident that the new controller proposed exhibits several advantages, a chief among them are the following:

- The considered DC-AC inverter is multi-level type, while the most previous studies were limited to the simple case of a two-level converter [15].
- The controller design is based on the nonlinear model representing the whole considered wind system. Therefore, it can ensure the expected performances over a wide range of loads variation. This is not the case for the linear controllers established in [19].
- The obtained performances, are formally established by using the tools of Lyaounov stability, unlike the case in [20]
- The construction of the harmonic current references is carried out by the instantaneous power technique (p&q theory). The latter has the advantage of being relatively fast and simple to be implemented. Unlike [21], where the construction of the current references was performed using the synchronous reference frame (d-q) technique. This technique achieves the desired harmonics compensation, but its implementation requires a high computational load, and its noise immunity depends on PLL and filter (LPF).
- The used modulation technique is the carrier-based sinusoidal pulse width modulation (SPWM). This latter provides a good compromise between simplicity of implementation and harmonic generation. This is not the case in [19], where the space vector pulse width modulation (SVPWM) is investigated to generate gate signals for the NPC inverter.

This paper is organized as follows: The grid connected wind system description is introduced in section 2, while the grid connected wind system modeling is developed in Section 3; Section 4 is devoted to the generation of reference signals; the controller synthesis and analysis are presented in section 5 and its performances are illustrated by simulation in Section 6; Section 7 concludes the paper.

2. GRID CONNECTED WIND SYSTEM DESCRIPTION

The present work focuses on the grid connected wind system described by Figures (1-2). This system consists of a three-phase AC grid, non-linear loads and a wind turbine generator connected to the network through an AC-DC converter and a DC-AC multilevel inverter. In fact, the AC-DC converter is used in order to track the maximum available wind power [3]. While the DC-AC three level NPC inverter is used for injecting the extracted rotor energy to the grid, as well as improving power quality by compensating the harmonic load currents and reactive power. Fig.2 shows that each arm of this inverter consists of four switches. The DC bus is fitted with a capacitive divider to provide two voltage sources of value $V_{dc}/2$. Consequently, the inverter AC voltage has three levels $(V_{dc}/2,\ 0,\ -V_{dc}/2)$. From the AC side, the NPC inverter is connected to the network through a filtering inductor (R, L) (see Fig.2) in order to reduce the circulation of the harmonics currents due to the inverter switching.

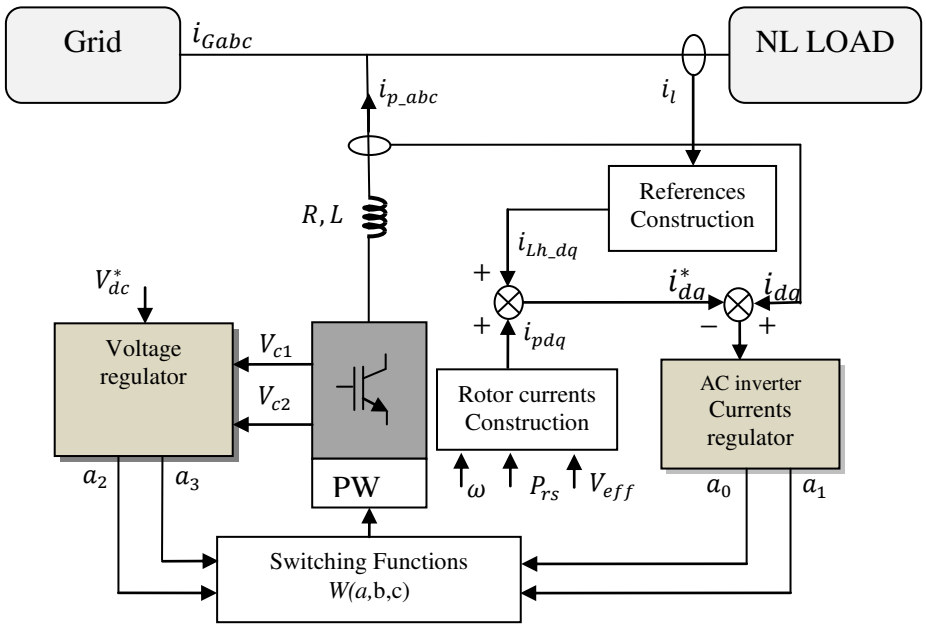

Figure-3. Block diagram of the GSC.

In order to produce gate signals for the NPC inverter, the unipolar sinusoidal pulse width modulation (SPWM) generator is considered. Recall that the principle of this modulation mode is to control each switch for one half modulating signal period and remain in a fixed state in the other half cycle [22]. So, only one capacitor is connected to the output per a half-cycle of the fundamental frequency. This modulation mode is preferred at high output frequencies. Moreover, the switching losses are lower in the unipolar mode. Figure-3 describes the operating principle of this modulation technique. Indeed, the switching function (W_j) of the three-level NPC inverter is defined as:

$$W_j = \begin{cases} 1, & \text{when } u_{j1} \text{ and } u_{j2} \text{ are conducting} \\ 0, & \text{when } u_{j2} \text{ and } \bar{u}_{j1} \text{ are conducting} \\ -1, & \text{when } \bar{u}_{j1} \text{ and } \bar{u}_{j2} \text{ are conducting} \end{cases}; \quad j = a, b, c \tag{1}$$

If V_{c1} and V_{c2} are equal, each switch has to tolerate only a half of the total DC link voltage. So, the output voltage of each leg can be expressed as follow:

$$v_{tj} = {}^{V_{dc}}/_{2} * W_j \quad ; \quad j = a, b, c \tag{2}$$

Another motivation behind equalizing V_{c1} and V_{c2} is to maintain the harmonic distortion of the terminal voltage at minimum. Any inequality between V_{c1} and V_{c2}, will lead to generate more harmonics in the terminal voltage of the NPC.

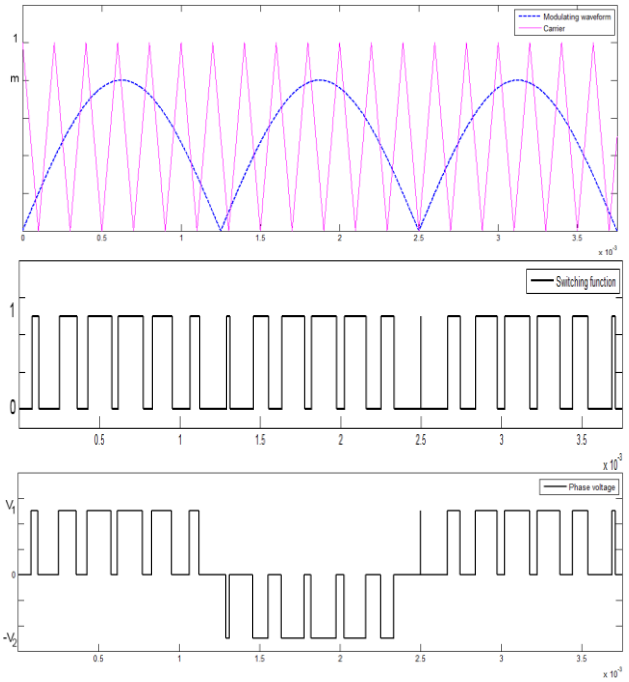

Figure-4. Unipolar PWM waveforms: (a) modulating signal/carrier (b) switching function W_a and (c) voltage v_{ta} in (Volt).

3. WIND SYSTEM MODELING

Based on the generalized state-space averaging method, to develop the 3 level NPC model some assumptions are crucial:

A.1. The carrier frequency is assumed much larger than the modulating signal frequency.

A.2. The Inverter switching and conduction losses are represented by series resistance on the grid side.

A.3. The non linear load as well as the utility grid are assumed to be balanced.

For the NPC modeling, let's consider for the phase a, the switching function W_a, where the NPC's voltage output can be expressed as $W_a V_{c1}$ during the first half-cycle of the modulating signal, and expressed as $-W_a V_{c2}$ during the second half-cycle of the modulating signal (see Figure-4). Recall that the considered PWM technique is the unipolar PWM. Accordingly, the switching function W_a can be expressed as:

$$W_a(t) = \overline{W_a} + harmonics \quad (3)$$

Where $\overline{W_a}$ is the average of $W_a(t)$ within one carrier period as illustrated in Figure-4. With assumption A.1, high frequency harmonics of the modulation signals can be neglected. Consequently, the average value of the switching function $W_a(t)$ (Figure-4) can be approximated by the instantaneous value of the modulating signal as follows:

$$W_a(t) = +a_0 \sin\left(\omega t + a_1 + \frac{\pi}{2}\right) + a_2 \text{ (first half-cycle)} \quad (4)$$

$$W_a(t) = -a_0 \sin\left(\omega t + a_1 + \frac{\pi}{2}\right) + a_3 \text{ (second h-c)} \quad (5)$$

where a_0, a_1 and ω are respectively the amplitude, the initial phase and the fundamental frequency of the modulated signal. $a_2$and a_3 are the DC offsets of the sinusoidal varying modulating waveform in each half-cycle. The angular frequency of the modulating signal is $\omega = 2\pi f_s$. To avoid over-modulation the following conditions are retained [22]:

$$0 \leq a_2 \leq 1 - a_0 \quad (6)$$

$$0 \leq a_3 \leq 1 - a_0 \quad (7)$$

Remark 1:

a) Recall that two pairs of switches of one leg receives inverted gate signals u_{ak} and $\bar{u}_{ak}$ $(k = 1, 2)$.

b) The switching function described in (4)-(5) concern the phase-a. For phase-b and phase-c, the corresponding switching functions W_b and W_c are respectively obtained by shifting W_a by $\frac{-2\pi}{3}$ and $\frac{-4\pi}{3}$.

c) Similarly, the inverter AC inverter currents and voltages ($i_{pabc}(t)$ and $v_{tabc}(t)$) will be approximated by their first harmonic. For example, the approximation of the inverter AC current phase-a leads to:

$$i_{pa}(t) = \langle i_{pa}\rangle_0 + \langle i_{pa}\rangle_{-1} e^{-j\omega t} + \langle i_{pa}\rangle_1 e^{j\omega t} \quad (8)$$

where $\langle i_{pa}\rangle_k$ $(k \in \{0, 1, -1\})$ are the Fourier series development coefficients■

By applying the usual electrical laws to the considered wind energy system, the NPC inverter dynamic can be described in the d-q frame by the following generalized average model [22].

$$\frac{d(V_{c1}-V_{c2})}{dt} = -\frac{3}{\pi C}\left(i_{pd}\, cos(a_1 + \omega t) + i_{pq}\, sin(a_1 + \omega t)\right)(a_2 - a_3) \quad (9)$$

$$\frac{d(V_{c1}+V_{c2})}{dt} = \frac{2}{C}\langle I_{dc}\rangle_0 - \frac{3}{2C}a_0\left(i_{pd}\, cos(a_1 + \omega t) + i_{pq}\, sin(a_1 + \omega t)\right) - \frac{3}{\pi C}(a_2 + a_3)\left(i_{pd}\cos(a_1 + \omega t) + i_{pq}\sin(a_1 + \omega t)\right) \quad (10)$$

$$\frac{di_{pd}}{dt} = -\frac{R}{L}i_{pd} + \omega i_{pq} - \frac{1}{L}V_{sd} + \frac{1}{L}\left[V_{c1}\left(\frac{a_0}{2} + \frac{2a_2}{\pi}\right) + V_{c2}\left(\frac{a_0}{2} + \frac{2a_3}{\pi}\right)\right] cos(a_1) \quad (11)$$

$$\frac{di_{pq}}{dt} = -\frac{R}{L}i_{pq} - \omega i_{pd} - \frac{1}{L}V_{sq} + \frac{1}{L}\left[V_{c1}\left(\frac{a_0}{2} + \frac{2a_2}{\pi}\right) + V_{c2}\left(\frac{a_0}{2} + \frac{2a_3}{\pi}\right)\right] sin(a_1) \quad (12)$$

For the above model, the following notations are retained:

$$I_{pd} = 2Re\{\langle i_{pa}\rangle_1\} \quad (13)$$

$$I_{pq} = 2Im\{\langle i_{pa}\rangle_1\} \quad (14)$$

$$V_{sd} = 2\, Re\{\langle V_{sa}\rangle_1\} \quad (15)$$

$$V_{sq} = 2\, Im\{\langle V_{sa}\rangle_1\} \quad (16)$$

$$a_1 = \left(\delta - \frac{\pi}{2}\right) \quad (17)$$

The state model defined by (9)-(12) can be rewritten in the more compact form given by:

$$\dot{x}(t) = f\left(x(t), u_p(t), w(t)\right) \quad (18)$$

where $x(t) = [(V_{c1} - V_{c2}) \quad (V_{c1} + V_{c2}) \quad i_{pd} \quad i_{pq}]^T$ is the state space vector, $w(t) = [V_{sd} \quad V_{sq}]^T$ is the measurable disturbances vector and $u_p(t) = [a_0 \quad a_1 \quad a_2 \quad a_3]^T$ is the virtual control vector. Equations (9) to (12) describe the dynamic behavior of the three-phase NPC of Figure-1, where all the notations are gathered in Table-1. Notice that if we assume $a_2 = a_3 = 0$, and C is replaced by 2C, the dynamic model of the three-level NPC, becomes the same model as that of the two-level [3], [5]. The assumption of $a_2 = a_3 = 0$ implies that no DC neutral-point current exists and the equivalent capacitance of the two capacitors becomes reduced to only one capacitor. This is an important outcome which permits

all the analytical techniques developed for the two-level converters, to be also applicable to the NPC [22].

Remark 2:

a) According to the virtual control vector $u_p(t)$, the actual switching functions are constructed in accordance with (4)-(5).

b) By performing the following NPC inverter voltages:

$$V_d = \left[V_{c1}\left(\frac{a_0}{2}+\frac{2a_2}{\pi}\right)+V_{c2}\left(\frac{a_0}{2}+\frac{2a_3}{\pi}\right)\right]\cos(a_1) \quad (19)$$

$$V_q = \left[V_{c1}\left(\frac{a_0}{2}+\frac{2a_2}{\pi}\right)+V_{c2}\left(\frac{a_0}{2}+\frac{2a_3}{\pi}\right)\right]\sin(a_1) \quad (20)$$

one can easily show that the control parameters a_1 and a_0 verify:

$$a_1 = \tan^{-1}\left(\frac{V_q}{V_d}\right) \quad (21)$$

and the modulating index:

$$a_0 = \frac{2}{V_{c1}+V_{c2}}\left(\sqrt{{V_d}^2+{V_q}^2}-\frac{2a_2}{\pi}V_{c1}-\frac{2a_3}{\pi}V_{c2}\right) \quad (22)$$

c) The model considered for DFIG is a state model widely used in the literature [23]. It is developed in a rotating reference frame (d-q) and oriented according to the stator flux direction ($\varphi_{sd} = \varphi_s ; \varphi_{sq} = 0$). The state space model is given by:

$$\begin{bmatrix}\dot{z}_1\\ \dot{z}_2\\ \dot{z}_3\\ \dot{z}_4\\ \dot{z}_5\end{bmatrix} = \begin{bmatrix}-\frac{a}{\sigma} & 0\\ 0 & -\frac{a}{\sigma}\\ 0 & 0\\ \frac{1}{\sigma L_r} & 0\\ 0 & \frac{1}{\sigma L_r}\end{bmatrix} u + \begin{bmatrix}\frac{1}{\sigma L_s}V_{sd}-\frac{R_s}{\sigma L_s}z_1+\frac{aR_r}{\sigma}z_4\\ \frac{1}{\sigma L_s}V_{sq}-\frac{R_s}{\sigma L_s}z_2+\frac{aR_r}{\sigma}z_5\\ -\frac{f}{J}z_3\\ -\frac{a}{\sigma}V_{sd}-\frac{R_r}{\sigma L_r}z_4+\frac{aR_s}{\sigma}z_1\\ -\frac{a}{\sigma}V_{sq}-\frac{R_r}{\sigma L_r}z_5+\frac{aR_s}{\sigma}z_2\end{bmatrix}$$

$$+\begin{bmatrix}\frac{M_{sr}}{\sigma L_s}pz_3z_5+\frac{1}{\sigma}(1-aM_{sr})\omega_s z_2+\frac{1}{\sigma}aM_{sr}pz_3z_2\\ -\frac{M_{sr}}{\sigma L_s}pz_3z_4-\frac{1}{\sigma}(1-aM_{sr})\omega_s z_1-\frac{1}{\sigma}aM_{sr}pz_3z_1\\ m\left(z_5\,z_1-z_4\,z_2\right)-\frac{T_a}{J}\\ -\frac{M_{sr}}{\sigma L_r}pz_3z_2-\frac{1}{\sigma}(aM_{sr}-1)\omega_s z_5-\frac{1}{\sigma}pz_3z_5\\ \frac{M_{sr}}{\sigma L_r}pz_3z_1+\frac{1}{\sigma}(aM_{sr}-1)\omega_s z_4+\frac{1}{\sigma}pz_3z_4\end{bmatrix} \quad (23)$$

where the state space vector and the control vector considered are respectively:

$$Z = [z_1\ z_2\ z_3\ z_4\ z_5]^T = [i_{sd}\ i_{sq}\ \Omega\ i_{rd}\ i_{rq}]^T \quad (24)$$

$$u = [V_{rd}\ V_{rq}\ ]^T \quad (25)$$

and the model parameters are:

$$a = \frac{M_{sr}}{L_r L_s}\ ; \sigma = 1-\frac{{M_{sr}}^2}{L_r L_s}\ ; m = -\frac{pM_{sr}}{J}; \beta = \frac{1-\sigma}{\sigma M_{sr}} \blacksquare \quad (26)$$

4. WIND SYSTEM CONTROLLER DESIGN

4.1 Control objectives reformulation

This paper focuses on the control design of the multi-level NPC inverter involved in the considered interfacing Wind/Grid system (see Figure-1. Indeed, the wind system control is carried out by injecting into the grid (through the NPC inverter) an AC current ($i_{pa,b,c}$,). Note that the fundamental component of the NPC AC currents takes into account the available the available wind power. Moreover, the harmonics components of this injected current are also controlled to compensate the reactive and harmonics components of the load current. This control objective ensures, even in the presence of non-linear load, a grid current practically sinusoidal with a unit power factor coefficient (PFC). Otherwise, in order that the NPC inverter operates properly, it is necessary to maintain the DC bus voltage (V_{dc}) at a suitable level and to balance the capacitor voltages (V_{c1}, V_{c2}).

For the grid connected wind system described in Figures (4-5), we seek the achievement of the following control objectives:

a) Controlling the transmitted wind power (P_{wind}) to the grid.

b) Regulating the DC bus voltage (V_{dc}) to maintain the capacitor charge at a suitable level.

c) Balancing the capacitor voltages (V_{c1}, V_{c2}).

d) Controlling the NPC AC current (i_{pd}, i_{pq}) for Compensating the reactive power and harmonic currents generated by the non linear load.

One difficulty with the problem at hand is that, there are four variables that need to be controlled (i.e. i_{pd}, i_{pq}, V_{dc} and $V_{c1}-V_{c2}$), while one only has two control inputs (i.e. the d and q components of the actual switching functions (W_{abc}). This is coped with by considering a cascade control strategy involving two loops (see Figure-4). The outer control loop aims to regulate the DC bus voltage and to balance the capacitor voltages (V_{c1}, V_{c2}). Indeed, the outer controller adjusts the DC components of the NPC inverter control signals (denoted (a_2 , a_3)) (see Figure-4). These resulting virtual control signals are then used to construct the desired fundamental active components (denoted (i_{pa} , i_{pb} , i_{pc})) of the output inverter current. These components, computed according to the available rotor power, are augmented with the load current harmonics and reactive components (next denoted (i_{hd} , i_{hq})), to constitute the final AC current references (i_d^* , i_q^*). The inner control loop aims to track the inverter AC current reference signals by adjusting the NPC inverter control parameters (a_0 , a_1). According to

(1)-(2), with the control vector parameters $[a_0 \quad a_1 \quad a_2 \quad a_3]^T$ one can compute the switching functions (W_{abc}) (see Figure-4).

4.2 Currents references signals' construction

a. Load current decomposition

The achievement of the fourth objective entails real time construction of the reference signals from harmonic and reactive load currents. Presently, this decomposition is performed using the so-called instantaneous power technique which enjoys an adequate compromise between accuracy and computational complexity [21]. Accordingly, the active and the reactive load powers can both be decomposed in a continuous and a varying component as follows:

$$\begin{bmatrix} P \\ Q \end{bmatrix} = \begin{bmatrix} \bar{p} + \tilde{p} \\ \bar{q} + \tilde{q} \end{bmatrix} = \begin{bmatrix} v_{s\alpha} & v_{s\beta} \\ -v_{s\beta} & v_{s\alpha} \end{bmatrix} \begin{bmatrix} i_{Lh\_\alpha} \\ i_{Lh\_\beta} \end{bmatrix} \quad (27)$$

Solving this equation with respect to the currents, and rearranging terms one easly gets the harmonic load current components:

$$\begin{bmatrix} i_{Lh\_\alpha} \\ i_{Lh\_\beta} \end{bmatrix} = \frac{1}{\Delta} \begin{bmatrix} v_{s\alpha} & -v_{s\beta} \\ v_{s\beta} & v_{s\alpha} \end{bmatrix} \begin{bmatrix} \bar{p} + \tilde{p} \\ \bar{q} + \tilde{q} \end{bmatrix} \quad (28)$$

With $\Delta = {v_{s\alpha}}^2 + {v_{s\beta}}^2$ (29)

Then, the harmonics components of the inverter output current references are given by:

$$\begin{bmatrix} i_{Lh\_\alpha} \\ i_{Lh\_\beta} \end{bmatrix} = \underbrace{\frac{1}{\Delta} \begin{bmatrix} v_{s\alpha} & -v_{s\beta} \\ v_{s\beta} & v_{s\alpha} \end{bmatrix} \begin{bmatrix} \tilde{p} \\ \tilde{q} \end{bmatrix}}_{\text{harmonic component}} + \underbrace{\frac{1}{\Delta} \begin{bmatrix} v_{s\alpha} & -v_{s\beta} \\ v_{s\beta} & v_{s\alpha} \end{bmatrix} \begin{bmatrix} 0 \\ \bar{q} \end{bmatrix}}_{\text{reactive component}} \quad (30)$$

In rotating synchronous reference frame d-q, using park transformation [22], the computed α-β current references (30) are transformed to (i_{Lh_d} , i_{Lh_q}).

b. Reference signals for the inverter output currents

The DFIG's main advantage is that it can be controlled only by the rotor side, which implies that the size of the converters is optimized, and the system's costs reduced. Nevertheless, the power still be generated by both stator and rotor sides. Accordingly, the extracted Power by the whole system to the grid is the sum of the stator's power and that of the rotor delivered through the 3levels NPC inverter:

$$P_W = P_{Rotor} + P_{Stator} \quad (31)$$

where the available electric power collected respectively at the DFIG stator and rotor are given by:

$$P_{Stator} = V_{sd} i_{sd} + V_{sq} i_{sq} \quad (32)$$

$$P_{Rotor} = V_{rd} i_{rd} + V_{rq} i_{rq} \quad (33)$$

Note that by substituting (32) and (33) in (31) one can easily compute the available aerodynamic power by measuring both rotor and stator DFIG voltages and currents.

Elsewhere, the available DFIG rotor power can be decomposed as

$$P_{Rotor} = P_{dc} + P_{pcc} \quad (34)$$

where P_{dc} and P_{pcc} denote respectively the consumed power at the DC bus (to ensure the balance and the regulation of the DC bus voltage) and the injected wind power at the PCC. In fact, under assumption A2, one has:

$$P_{pcc} = V_{td} i_{pd} + V_{tq} i_{pq} = \left(V_{sd} i_{pd} + V_{sq} i_{pq}\right) + \underbrace{R\left(i_{pd}^2 + i_{pq}^2\right)}_{\substack{\text{Joule losses at} \\ \text{the coupling filter}}} \quad (35)$$

$$P_{dc} = \underbrace{C\frac{d(V_{c1}+V_{c2})}{dt}}_{P_{ch}} + \underbrace{C\frac{d(V_{c1}-V_{c2})}{dt}}_{P_{bal}} \quad (36)$$

where P_{ch} and P_{bal} denote respectively to the required power for adjusting the DC bus voltage and for balancing the capacitor voltages.

By substituting (9) and (10) in equation (36) one can easily has:

$$P_{dc} = 2\langle I_{dc} \rangle_0 - \frac{3}{2} a_0 \left(i_{pd} \cos(a_1) + i_{pq} \sin(a_1)\right) - \frac{6}{\pi} \left(i_{pd} \cos(a_1) + i_{pq} \sin(a_1)\right) a_2 \quad (37)$$

Now by substituting (32)-(36) in (31), the available electrical power collected in the rotor side at the PCC (denoted by P_{rs}) is given by:

$$P_{rs} = P_w - P_{Stator} - P_{dc} - R\left(i_{pd}^2 + i_{pq}^2\right) \quad (38)$$

With equation (38), one can easily deduce the reference signals for the fundamental components ($i_{pa\_f} \quad i_{pb\_f} \quad i_{pc\_f}$) for the injected current at the PCC. Indeed, with $\omega = 2\pi f_s \ (rad/s)$ one has:

$$i_{pa\_f} = \frac{P_{rs}}{3V_{eff}} \sqrt{2} \cos(\omega t) \quad (39)$$

$$i_{pb\_f} = \frac{P_{rs}}{3V_{eff}} \sqrt{2} \cos\left(\omega t + \frac{2\Pi}{3}\right) \quad (40)$$

$$i_{pc\_f} = \frac{P_{rs}}{3V_{eff}} \sqrt{2} \cos\left(\omega t + \frac{4\Pi}{3}\right) \quad (41)$$

In rotating synchronous reference frame d-q, using park transformation [22], the computed three phases current references (39)-(41) are transformed to (I_{pd_f} , I_{pq_f})

Finally, in the d-q reference frame, the global reference signals for the inverter output currents (denoted respectively ${i_{pd}}^*$ and ${i_{pq}}^*$) are given by adding the reference signals for the fundamental components

(I_{pd_f}, I_{pq_f}) with the harmonics components (I_{Lh_d}, I_{Lh_q}):

$$\begin{bmatrix} i_{pd}^{*} \\ i_{pq}^{*} \end{bmatrix} = \begin{bmatrix} i_{Lh\_d} \\ i_{Lh\_q} \end{bmatrix} + \begin{bmatrix} i_{pd\_f} \\ i_{pq\_f} \end{bmatrix} \quad (42)$$

4.3 Inner control loop design

The inner current control loop is designed to track the current references (i_{pd}^{*}, i_{pq}^{*}) (see Figure-3). This loop must be able to make the following current tracking errors as small as possible:

$$z_1 = i_{pd} - i_{pd}^{*} \quad (43)$$

$$z_2 = i_{pq} - i_{pq}^{*} \quad (44)$$

It follows by using the model (11) and (12) that the errors time derivatives undergo the following equation:

$$\begin{bmatrix} \dot{z}_1 \\ \dot{z}_2 \end{bmatrix} = -\frac{R}{L}\begin{bmatrix} i_{pd} \\ i_{pq} \end{bmatrix} + \omega \begin{bmatrix} i_{pq} \\ -i_{pd} \end{bmatrix} - \frac{1}{L}\begin{bmatrix} V_{sd} \\ V_{sq} \end{bmatrix} + \frac{1}{L}\begin{bmatrix} V_d \\ V_q \end{bmatrix} - \begin{bmatrix} \dot{i}_{pd}^{*} \\ \dot{i}_{pq}^{*} \end{bmatrix} \quad (45)$$

where the virtual control signals V_d and V_q are respectively defined by (19)-(20).

For stability analysis of the tracking error system (43)-(44), consider the following Lyapunov candidate function:

$$V_i = \frac{1}{2}z_1^2 + \frac{1}{2}z_2^2 \quad (46)$$

By using (45), time derivative of the Lyapunov candidate function (46) is given by:

$$\dot{V}_i = \begin{bmatrix} z_1 \\ z_2 \end{bmatrix}^T \left(-\frac{R}{L}\begin{bmatrix} i_{pd} \\ i_{pq} \end{bmatrix} + \omega \begin{bmatrix} i_{pq} \\ -i_{pd} \end{bmatrix} - \frac{1}{L}\begin{bmatrix} V_{sd} \\ V_{sq} \end{bmatrix} + \frac{1}{L}\begin{bmatrix} V_d \\ V_q \end{bmatrix} - \begin{bmatrix} \dot{i}_{pd}^{*} \\ \dot{i}_{pq}^{*} \end{bmatrix} \right) \quad (47)$$

To ensure the asymptotic stability of the equilibrium $(z_1, z_2) = (0, 0)$, equation (47) suggests that the virtual controls (V_d, V_q) should be chosen so that:

$$\begin{bmatrix} -k_1 z_1 \\ -k_2 z_2 \end{bmatrix} = -\frac{R}{L}\begin{bmatrix} i_{pd} \\ i_{pq} \end{bmatrix} + \omega \begin{bmatrix} i_{pq} \\ -i_{pd} \end{bmatrix} - \frac{1}{L}\begin{bmatrix} V_{sd} \\ V_{sq} \end{bmatrix} + \frac{1}{L}\begin{bmatrix} V_d \\ V_q \end{bmatrix} - \begin{bmatrix} \dot{i}_{pd}^{*} \\ \dot{i}_{pq}^{*} \end{bmatrix} \quad (48)$$

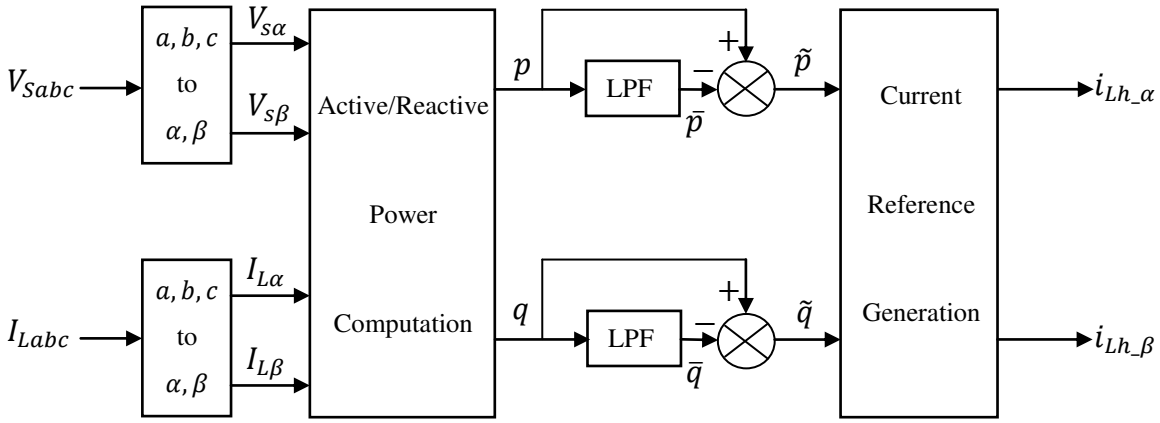

Figure-5. Instantaneous power theory scheme.

where k_1, k_2 are any real positive control design parameters.

Solving (48) with respect to (V_d, V_q) yields the following virtual control:

$$\begin{bmatrix} V_d \\ V_q \end{bmatrix} = L\begin{bmatrix} -k_1 z_1 \\ -k_2 z_2 \end{bmatrix} + R\begin{bmatrix} i_{pd} \\ i_{pq} \end{bmatrix} - L\omega \begin{bmatrix} i_{pq} \\ -i_{pd} \end{bmatrix} + \begin{bmatrix} V_{sd} \\ V_{sq} \end{bmatrix} + L\begin{bmatrix} \dot{i}_d^{*} \\ \dot{i}_q^{*} \end{bmatrix} \quad (49)$$

Using (49), the virtual AC current control parameters a_1 and a_0 are respectively computed by (21-22).

4.4 Outer control loop design:

The outer loop aims at making the voltage tracking errors:

$$z_3 = (V_{c1} - V_{c2}) - V_n^{*} \quad (50)$$

$$z_4 = (V_{c1} + V_{c2}) - V_{dc}^{*} \quad (51)$$

as small as possible, where the reference signal V_n^{*} is kept equal to zero for balancing the DC voltages (V_{c1}, V_{c2}), and V_{dc}^{*} is the reference value of the DC bus voltage.

With the tracking errors system given by (50)-(51), the considered sliding surface is defined by

$$S = \begin{bmatrix} S_1 \\ S_2 \end{bmatrix} = \begin{bmatrix} k_{30} z_3 + \int k_{33} z_3 \\ k_{40} z_4 + \int k_{44} z_4 \end{bmatrix} \quad (52)$$

where $(k_{30}, k_{33}, k_{40}, k_{44})$ are any real positive control design parameters. By using (9) and (10), time derivative of the considered sliding surface (52) is given by:

$$\dot{S} = D\begin{bmatrix} (\alpha_0 - \beta_0) \\ (\alpha_0 + \beta_0) \end{bmatrix} + F \quad (53)$$

Where

$$D = \begin{bmatrix} -\frac{3k_{30}}{\pi C}\left(i_{pd}\cos(a_1)\right) & 0 \\ 0 & -\frac{3k_{40}}{\pi C}\left(i_{pd}\cos(a_1)\right) \end{bmatrix}$$

$$+\begin{bmatrix} -\frac{3k_{30}}{\pi C}\left(i_{pq}\sin(a_1)\right) & 0 \\ 0 & -\frac{3k_{40}}{\pi C}\left(i_{pq}\sin(a_1)\right) \end{bmatrix} \quad (54)$$

and

$$\mathrm{F} = \begin{bmatrix} \mathrm{k_{33}(V_{c1} - V_{c2})} \\ \mathrm{k_{40}\frac{2}{C}\langle I_{dc}\rangle_0 - k_{40}\frac{3}{2C}a_0\left(i_{pd}\cos(a_1) + i_{pq}\sin(a_1)\right)} \end{bmatrix} - \\ -\begin{bmatrix} 0 \\ -k_{40}\dot{V}_{dc}^{*} + k_{44}(V_{c1} + V_{c2}) - k_{44}V_{dc}^{*} \end{bmatrix} \quad (55)$$

Equation (53) shows that the sliding surface S can be controlled with the virtual vector input $[a_2 \quad a_3]^T$. In the first step, the objective is to determine the considered control vector for ensuring the attractiveness and invariance of the surface S = 0. To this end, let consider the Lyapunov candidate function:

$$\mathrm{V_o} = \frac{1}{2}S^T S \quad (56)$$

By using (53), time derivative of the Lyapunov candidate function (56) is given by:

$$\dot{\mathrm{V}}_\mathrm{o} = S^T\dot{S} = S^T\left(F + D\begin{bmatrix} a_2 - a_3 \\ a_2 + a_3 \end{bmatrix}\right) \quad (57)$$

Equation (57) suggests choosing the virtual control vector $[a_2 \quad a_3]^T$ such that:

$$\begin{bmatrix} a_2 - a_3 \\ a_2 + a_3 \end{bmatrix} = -D^{-1}F - D^{-1}\begin{bmatrix} d_{10}sgn(S_1) \\ d_{20}sgn(S_2) \end{bmatrix} \quad (58)$$

where (d_{10}, d_{20}) are real positive constants.

Remark 3:

a) The virtual control law proposed in (58) assumes that the matrix D is invertible. In fact, $det(D) = \frac{9k_{33}k_{44}}{\pi^2C^2}\left(I_{pd}\,cos(a_1) + I_{pq}\,sin(a_1)\right)^2$ is greater than or equal to zero. To avoid any singularity, the computation of $det(D)$ has been slightly modified in accordance with:

$$det(D) = \frac{9k_{33}k_{44}}{\pi^2C^2}\left(I_{pd}\,cos(a_1) + I_{pq}\,sin(a_1)\right)^2 + \varepsilon,$$

where ε is a small positive constant.

b) By using equations (4-5), the virtual control vector $[a_2 \quad a_3]^T$ is used for constructing the NPC actual control (i.e. switching functions (W_{abc}))■

The theoretical performances of the closed-loop control are described in the next theorem

Theorem:

Consider the closed loop system composed of the grid connected three phase 3-level NPC inverter represented by the model (9)-(12), and the cascade nonlinear controller including:

- The AC current controller defined by (21) and (22).
- The DC voltage controller defined by (58).

For any real positive design parameters $k_1, k_2, k_{30}, k_{33}, k_{40}$ and k_{44}, one has the following results:

a) The AC current tracking errors (z_1, z_2) vanish exponentially fast.

b) The DC voltage tracking errors (z_3, z_4) vanish exponentially fast■

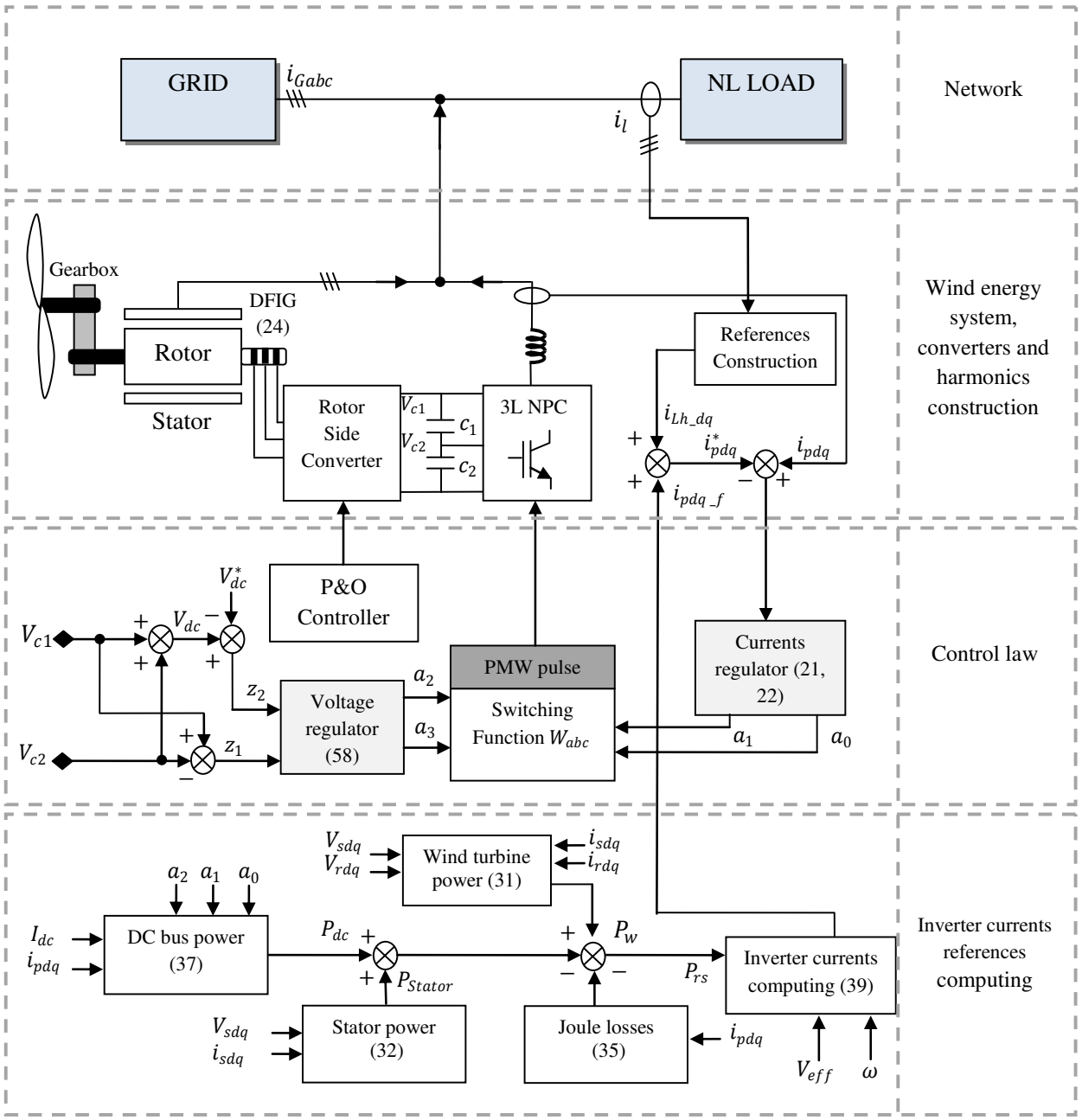

Figure-6. Whole proposed control strategy.

Proof of the theorem:

Part1: By substituting (49), in (48), one can easily show that:

$$z_1(t) = z_1(0)e^{-k_1 t},\ z_2(t) = z_2(0)e^{-k_2 t} \quad (59)$$

This proves that the AC current tracking errors system is globally and exponentially stable.

Part2: By substituting (58), in (57), one gets:

$$\dot{V}_o = -S^T \begin{bmatrix} d_1 \mathrm{sgn}(S_1) \\ d_2 \mathrm{sgn}(S_2) \end{bmatrix} = -d_{10}\mathrm{sgn}(S_1) - d_{20}\mathrm{sgn}(S_2) < 0 \quad (60)$$

By using Lyapunov's stability tools, equation (60) proofs part 2 of the theorem□

5. SIMULATIONS RESULTS

5.1 Simulation protocole

The simulations are realized on MATLAB/Simulink environment. The considered grid connected wind system is that described in Figure-1. Indeed, the DFIG generator is connected to the network through a DC/DC converter and a DC/AC multilevel inverter (3-level NPC inverter). The latter operates according to the PWM principle with a switching

frequency of 8 kHz. The nonlinear load and wind system characteristics are summarized in Table-2.

In this section, for the considered DC/AC multilevel inverter, the proposed control system is evaluated. To assess the control system performances in different operation points, the wind speed is made variable, according to the profile described by Figure-6. In fact, the simulation protocol is designed in such a way to consider a wide range variation of the wind speed [6-15m/s] see Figure-7. For the simulation, the DFIG generator is simulated based on its classical model [3]. The corresponding Power/ Rotor-Speed characteristic is presented in Figure-8

The AC/DC converter control (ensuring the MPPT objective) is performed using P&O algorithm [24]. The resulting optimal wind power is presented in Figure-9.

Elsewhere, the considered non-linear load is a three phases commanded converter associated to an RL load (see Table-3). To evaluate the performances of the developed controllers in different operation points, the load resistance (R_c) is made variable, according to the profile described in Figure-10. The resulting load power and current are respectively illustrated in Figure-11 and Figure-12. The harmonic load current spectra and the corresponding THD value are presented in Figure-13. Several tests will be performed to evaluate the robustness of the proposed wind system controller (load variation, grid faults and frequency deviation).

Table-2. Electrical machine parameters.

Electrical parameters	Index	Value
Stator/Rotor resistance	Rs/ Rr	0.455/0.62Ω
S/Rotor leakage inductance	Ls/ Lr	0.0083/0.0081H
Magnetizing inductance	Msr	0.0078H
Inertia	J	0.3125kgm^2
Viscous friction	F	6.73×10−1Nms−1

Table-3. Nonlinear load's Rectifier parameters.

Rectifier parameters	Index	Value
Rectifier inductance	L_c	1e^{-2} H
Rectifier resistance	R_c	10 Ω

Table-4. NPC inverter parameters.

inverter parameters	Index	Value
Inverter inductance	L	2e^{-3}
Inverter capacity	C	6.6e^{-6}
Inverter resistance	R	12e^{-3}

Table-5. NPC controller's parameters.

Index	Value	Index	Value
k_{30}	10	d_{10}	900
k_{40}	0.00001	d_{20}	1000
k_{33}	1e^{-3}	k_1	7e^5
k_{44}	1e^{-7}	k_2	7e^5

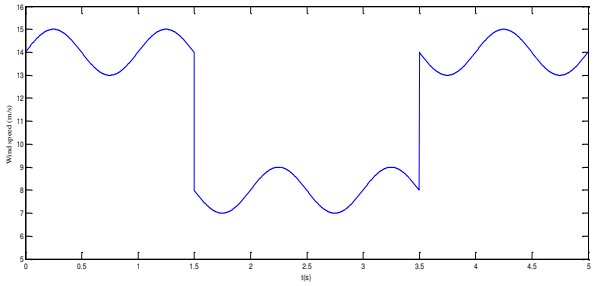

Figure-7. Wind speed profile.

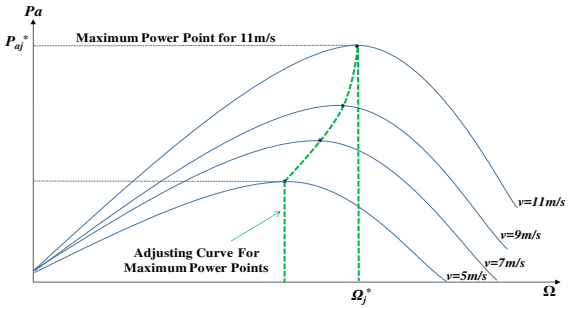

Figure-8. The shape of the aerodynamic power according to the rotor speed for various values of wind speed. Highlighting of MPP.

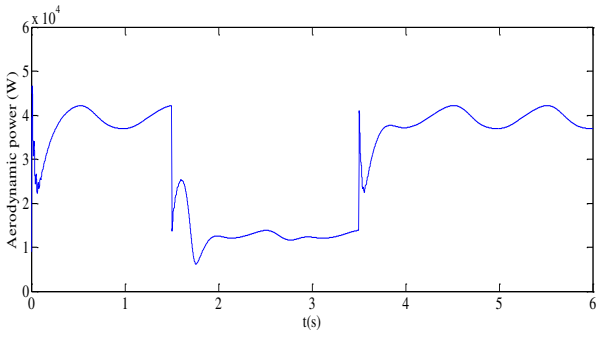

Figure-9. Aerodynamic power extracted from the wind turbine.

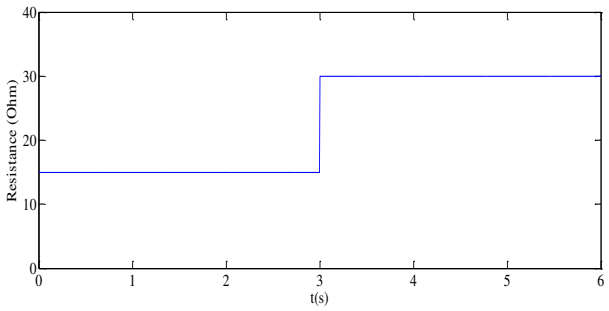

Figure-10. Load resistance variation profile.

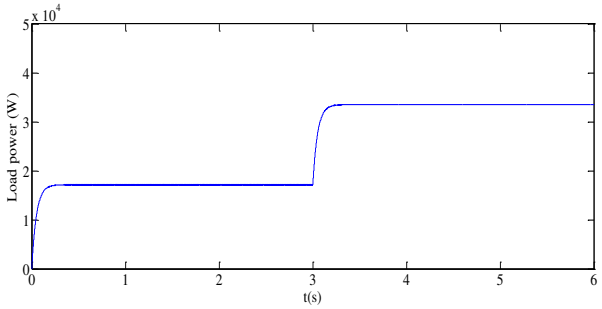

Figure-11. The shape of the load power.

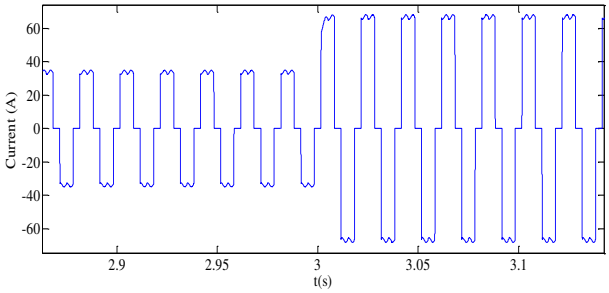

Figure-12. Load current (i_{la}) in time domain.

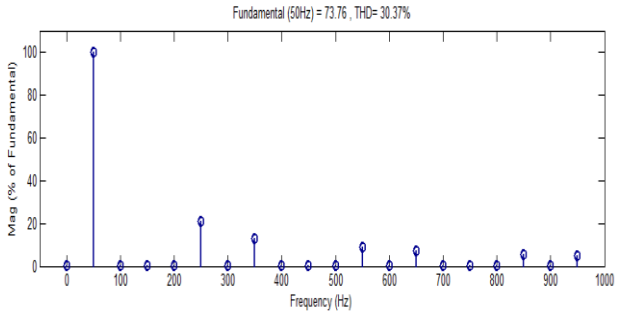

Figure-13. Load current in frequency domain.

5.2 Controller evaluation

The proposed control system includes the inverter AC current control loop (21)-(22) and the DC voltage control loop (58). The corresponding design parameters are given in table 3, which proved to be convenient. In this respect, note that there is no systematic way, especially in nonlinear control, to make suitable choices for these values. Therefore, the usual practice consists at proceeding with trial-error approach. By doing so, the numerical values (given in table 3) are retained.

5.2.1 Inner loop evaluation

Recall that for the inner loop, the AC current signal references $\left(I_{pd}^{*}, I_{pq}^{*}\right)$ are given by (42). The resulting controller performances are illustrated by Figures (15)-(16). In fact, Figure-15 and Figure-16 show that, independently of the load current or wind speed level, the inverter output AC currents track well their references, confirming the results of theorem.

According to the considered wind speed profile, Figure-14a shows the shape of the extracted wind power recovered at the AC side of the inverter. Indeed, during low wind speed, the wind system and the electrical network have contributed both to satisfy the load power (see Figure-14(a-b)). However, for a large value of the wind speed (i.e. for $t \in [0s\ 1.5s]$), the wind power contribution is greater enough than the variable load power (see Figure-14a). In this case, the excess generated wind power is evacuated to the grid that becomes an electrical receiver (see Figure-14b). However, from $t = 3s$ the nonlinear load value rises to $30\ \Omega$ according to the load profile (see Figure-10). So, from this time, the wind system and the electrical network contribute both to satisfy the increasing load power. According to the considered wind profile, the wind system provides approximately 137% of the energy requested by the proposed load.

On the other hand, recall that the AC current reference signals includes components for compensating load current harmonics. With the proposed controller, the resulting grid current is plotted in Figure-17. This figure shows that, unlike the load current and wind speed variation, the grid current is clean of harmonics. This is better illustrated by Figure-18, which shows the spectra of this current. It is seen that the network current is mainly constituted by a single component located in $50\ Hz$. The interest of the proposed controller is carried out by the obtained small values of the grid current THD compared to the load current THD (1,73% rather than 30,73%). This confirms that the wind system can also contribute greatly in improving the quality of the distributed energy

Furthermore, Figure-19 shows that for low wind velocity ($P_{wind} < P_{load}$), the proposed controller forces the network current to be in phase with the line voltage. Similarly, the same figure shows that for the large wind velocity ($P_{wind} > P_{load}$), the proposed controller forces the network current to be in phase opposition with the line voltage. This confirms the perfect compensation of the load reactive power (whatever the load nature or the wind velocity).

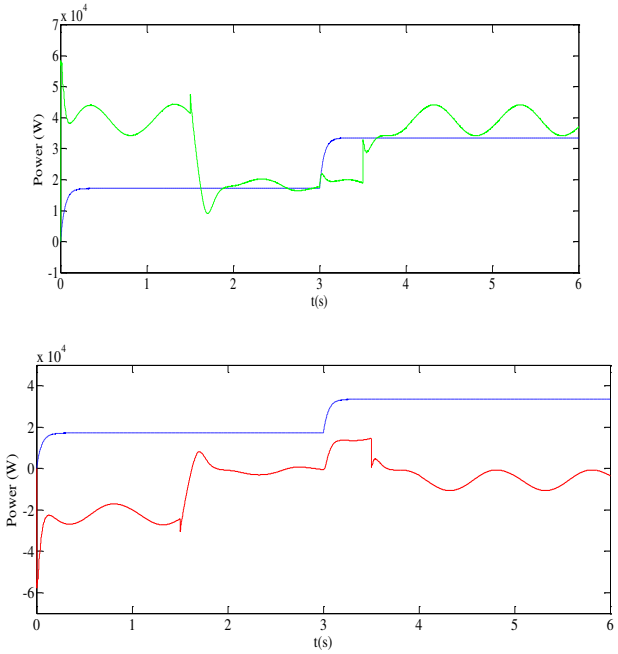

Figure-14a. Solid line: wind turbine power, dotted line: load power.

Figure-4b Solid line: Network Power, Dotted line: load power.

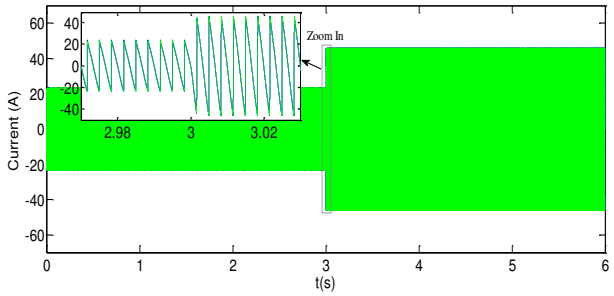

Figure-15. Solid line: d-component of the NPC inverter output current. Dotted line: its reference.

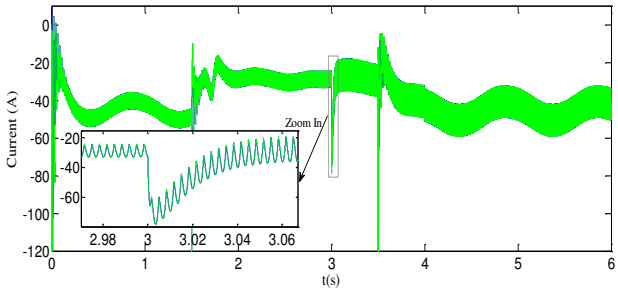

Figure-16. Solid line: q-component of the NPC inverter output current. Dotted line: its reference.

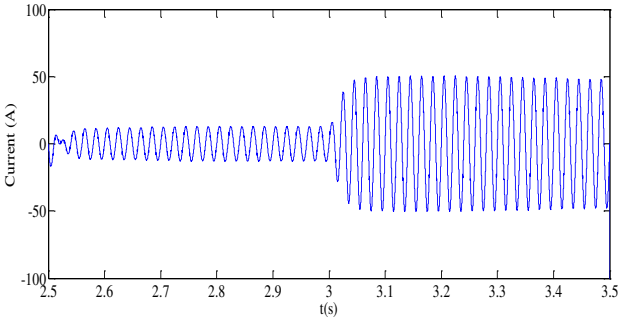

Figure-17. Network current (i_{sa}) with second load addition (at time 3s).

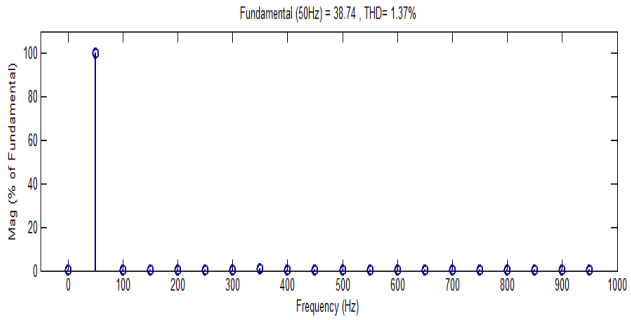

Figure-18. Network current after filtering in frequency domain.

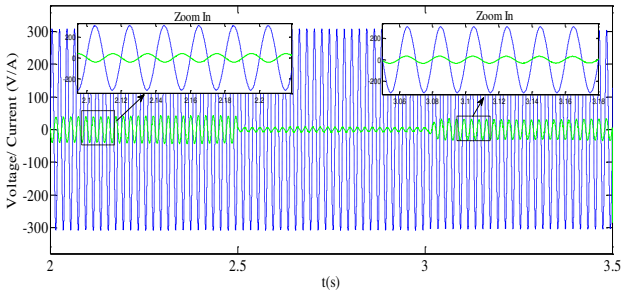

Figure-19. Dotted line: network voltage, solid line: network current.

5.2.2 Outer loop evaluation

Recall that the outer loop is dedicated firstly to maintain the DC bus voltage on a suitable reference value and also to balance the capacitors voltages (V_{c1}, V_{c2}). To this end, the outer loop voltage references (V_{dc_ref}, V_n^*) are respectively kept equal to $1000\ V$ and $0\ V$.

The resulting outer controller performances are illustrated by Figures 20-22. Indeed Figure-20 shows that the DC voltage tracks well its reference signal. Likewise Figure-21 shows that the potential difference $V_{c1} - V_{c2}$ exponentially vanishes. Figures 20-21 proves that the inverter's DC voltages (V_{c1}, V_{c2}) track well their references, confirming the results of Theorem 1. Note that despite the load value variation at time (3s), the regulators' performances are maintained. Furthermore Figure-22 shows the shape of the inverter output AC voltage, where three voltage levels are highlighted.

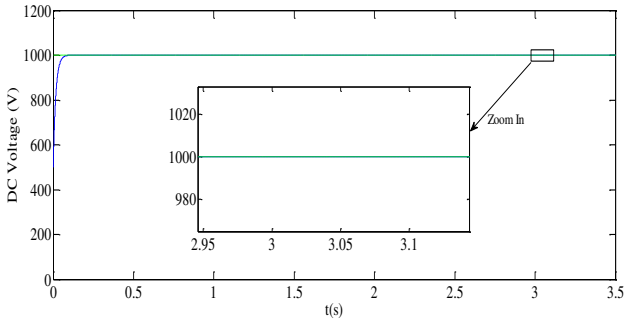

Figure-20. Solid line: DC voltage. Dotted line: its reference.

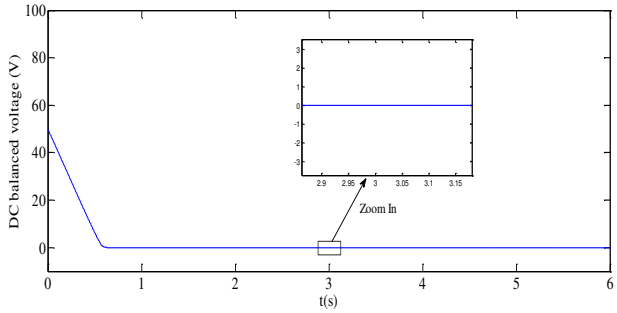

Figure-21. Balancing of the NPC DC capacitor voltages $[V_{c1} - V_{c2}]$.

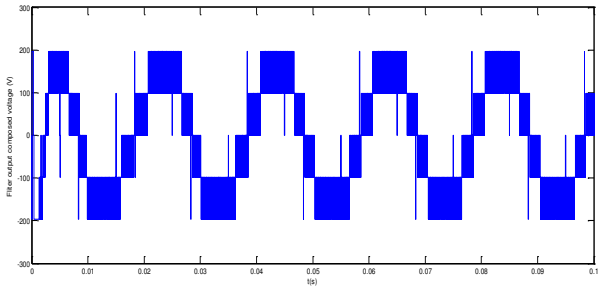

Figure-22. Zoom of the output voltage of 3 levels NPC inverter at time 0.1s.

5.3 Controller robustness evaluation

To evaluate the robustness of the proposed regulator, several tests were performed. Indeed, these tests aim to check whether the controller's performances are conserved even in the presence of grid faults or under frequency variation. These tests are classified into two parts: robustness under voltage dips and robustness despite the frequency variation.

5.3.1 Robustness under voltage dips

The robustness of the proposed controllers is tested under grid faults. The considered fault is a 3 phase voltage dip, which reduces the main voltage value of about 60% and last for 1s [1.9s-2.9s] as presented in Figure-23. Figure-24 presents the generated wind power, respectively in presence and absence of the considered voltage dip.

This figure shows that the produced wind power is slightly affected by the considered grid fault. Indeed there is a power drop of around 25%.

The resulting tracking errors of the inverter output currents are illustrated in Figures 25-26. These figures show that the tracking performances are practically insensitive to the considered voltage dip.

The shape of the grid current (presented in Figure-27) attests that despite the voltage dip the filtering objective remains achieved. Similarly, the resulting DC voltages control performances are illustrated in Figures 28-29. These figures also shows that the outer loop tracking performances are practically unaffected by the considered voltage dip.

This proves the good behavior of the proposed regulator in the presence of grid voltage dips.

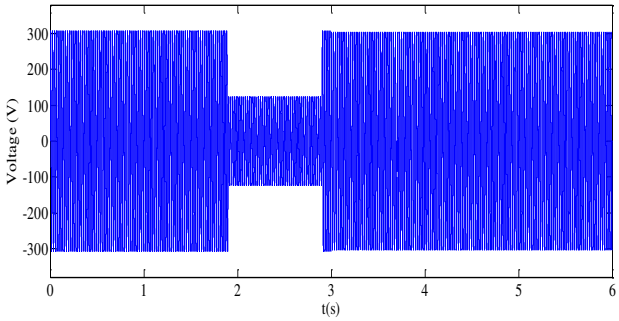

Figure-23. Network voltage under voltage dips.

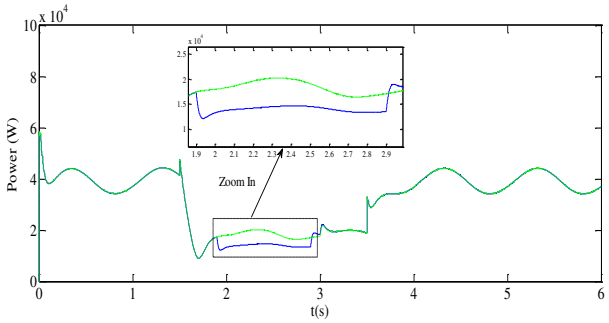

Figure-24. Solid line: wind turbine power under voltage dips. Dotted line: Wind turbine Power without voltage dips.

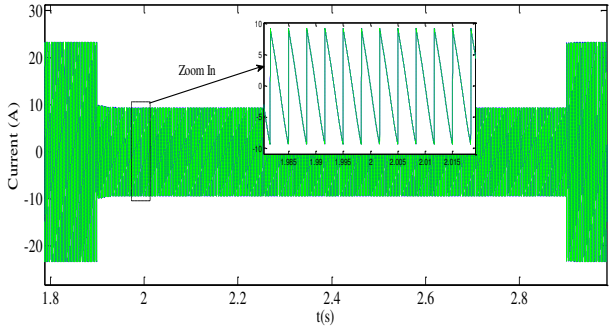

Figure-25. Solid line: d-component of the NPC inverter output current. Dotted line: its reference.

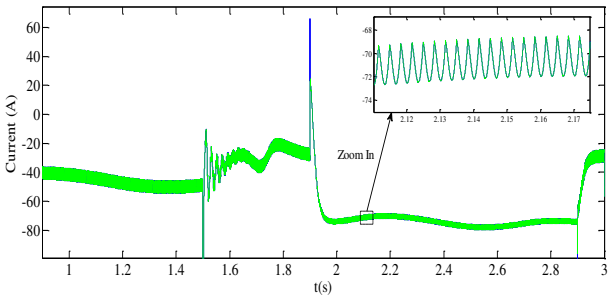

Figure-26. Solid line: q-component of the NPC inverter output current. Dotted line: its reference.

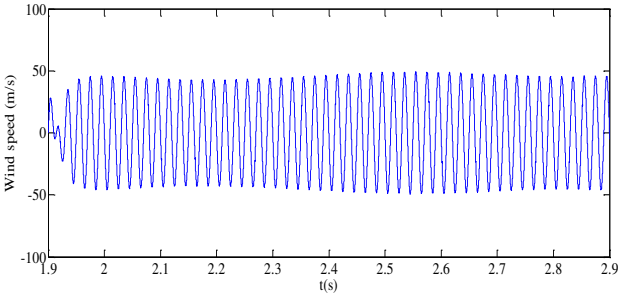

Figure-27. Zoom of the network current (i_{sa}) at voltage dip implementation (at time 1.9s).

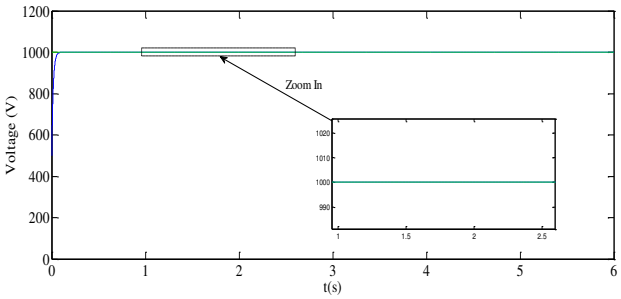

Figure-28. Solid line: DC voltage. Dotted line: its reference.

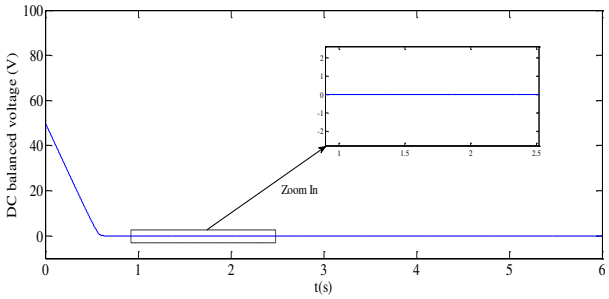

Figure-29. Balancing of the NPC DC capacitor voltages $[V_{c1} - V_{c2}]$.

5.3.2 Robustness under grid frequency variation

This test was carried out by considering a frequency variation [50-50.2 Hz]. The considered grid fault is introduced at time 3.7s and last for 1s as shown in Figure-30.

Figure-31 presents the generated wind power, respectively in presence and absence of the considered grid frequency variation. This figure shows that the produced wind power is not affected by the considered grid fault. Figures 32-33 show that despite the frequency variation, the tracking current objectives remain achieved with high accuracy. The shape of the grid current (presented in Figure-34) attests that despite the grid frequency variation, the filtering objective remains also reached. Furthermore, the resulting DC voltages control performances are presented in Figures 35-36. These figures also show that the outer loop tracking performances are practically unaffected by the considered grid frequency variation.

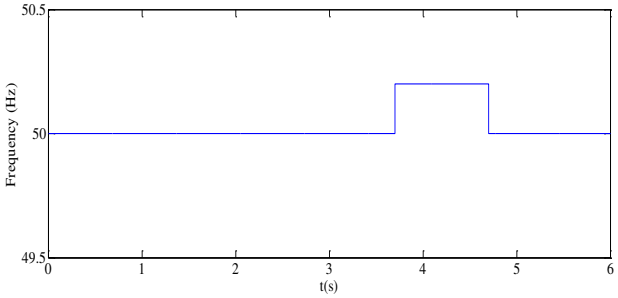

Figure-30. Network frequency profile.

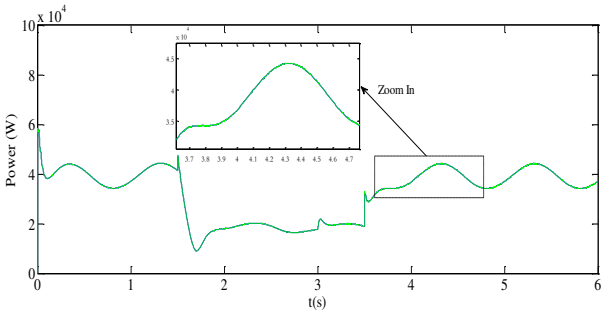

Figure-31. Solid line: Wind turbine power under frequency variation. Dotted line: Wind turbine Power without frequency variation.

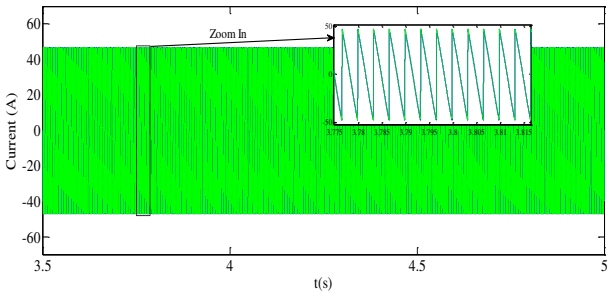

Figure-32. Solid line: d-component of the NPC inverter output current. Dotted line: its reference.

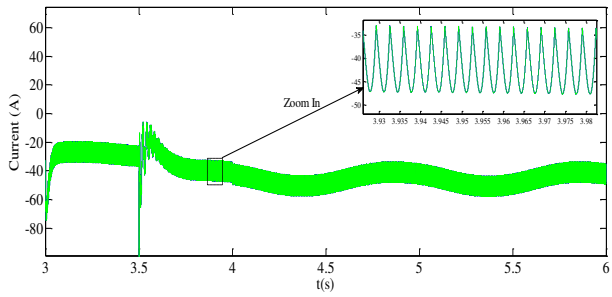

Figure-33. Solid line: q-component of the NPC inverter output current. Dotted line: its reference.

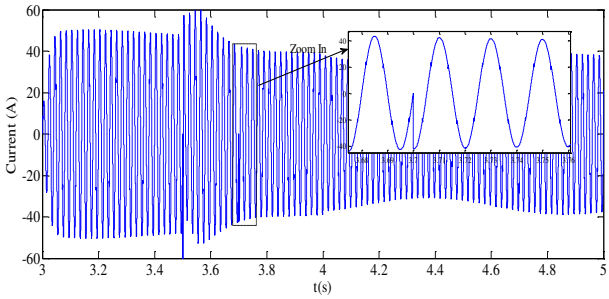

Figure-34. Zoom of the network current (i_{sa}) at frequency variation (at time 3.7s).

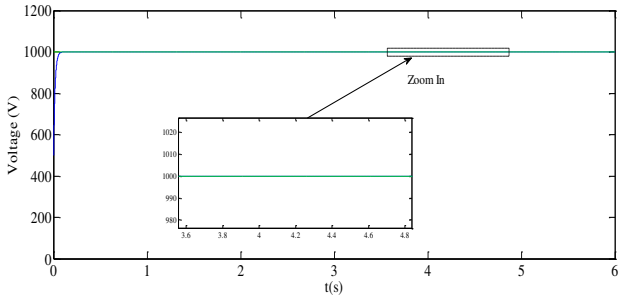

Figure-35. Solid line: DC voltage. Dotted line: its reference.

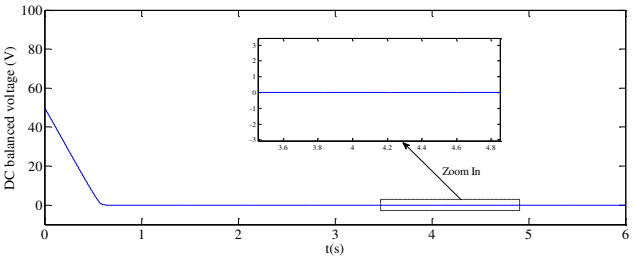

Figure-36. Balancing of the NPC DC capacitor voltages $[V_{c1} - V_{c2}]$.

6. CONCLUSIONS

This paper was dedicated to the design of a new controller for connecting a wind energy system based on a DFIG to the grid. The GSC that has been considered is a multi-level. Indeed, compared with the conventional structure with two levels, the considered topology introduces a lower harmonic distortion. The control objectives were threefold: (i) ensuring the transit of the generated power through the rotor side, (ii) regulating the DC bus voltage and its balance and (iii) cancelling the current harmonics generated by the nonlinear load. To meet these objectives, a nonlinear controller was built on the bases of the average state model of the NPC inverter (23). Interestingly, the DC bus voltage regulation and balance purposes were insured by a new sliding mode controller (58). While the inverter output currents control were performed using a backstepping technical (21)-(22). Using tools from Lyapunov's stability, it was formally shown that the closed-loop controllers systems, expressed in terms of the tracking errors, enjoys a global stability. These theoretical results were confirmed by simulations involving wide range variation of the wind speed. The robustness of the proposed regulators was also evaluated through several tests. Indeed, this allowed checking that the proposed controller maintains its good performances despite a grid frequency variation or under voltage dips.

On the basis of the above description, it is evident that the proposed controller exhibits several advantages, a chief among them are: the considered DC-AC inverter is multi-level type (while the most previous studies were limited to the simple case of a two-level converter e.g. [15]), the controller design is based on the nonlinear model representing the whole considered wind system (which is not the case for the linear controllers established in e.g. [19]), The proposed wind system contributes greatly in improving the quality of the distributed energy (by compensating the load harmonic current).

REFERENCES

[1] Schallenberg-Rodriguez J. 2013. A methodological review to estimate techno-economical wind energy production. Renewable and Sustainable Energy Reviews. 21: 272-287.

[2] Justo J.J, Mwasilu F and Jung J.W. 2015. Doubly fed induction generator based wind turbines: a comprehensive review of fault ride through strategies. Renewable and sustainable energy reviews. 45: 447-467.

[3] Yang B, Jiang L, Wang L, Yao W and Wu Q. H. 2016. Nonlinear maximum power point tracking control and modal analysis of DFIG based wind turbine. International Journal of Electrical Power & Energy Systems, 74, 429-436.

[4] Bezza M, Moussaoui B. E. L and Fakkar A. 2012. Sensorless MPPT fuzzy controller for DFIG wind turbine. Energy Procedia. 18, 339-348.

[5] Patin N. 2015 Introduction to Multi-level Converters. Power Electronics Applied to Industrial Systems and Transports, Volume 2. Power Converters and their Control. pp. 193-213.

[6] Seixas M, Melício R and Mendes V.M.F. 2014. Offshore wind turbine simulation: multibody drive train. Back-to-back NPC (neutral point clamped) converters. Fractional-order control. Energy. 69: 357-369.

[7] Subsingha W. 2016. Design and Analysis Three Phase Three Level Diode-Clamped Grid Connected Inverter. Energy Procedia. 89: 130-136.

[8] Merahi F and Berkouk E. M. 2013. Back-to-back five-level converters for wind energy conversion system with DC-bus imbalance minimization. Renewable Energy, 60: 137-149.

[9] Lai J. S and Peng F. Z. 1996. Multilevel converters-a new breed of power converters. Industry Applications, IEEE Transactions on. 32(3): 509-517.

[10] Colak I, Kabalci E, and Bayindir R. 2011. Review of multilevel voltage source inverter topologies and control schemes. Energy Conversion and Management 52: 1114–1128.

[11] [11] Nathenas T and Adamidis G. 2012. A new approach for SVPWM of a three-level inverter-induction motor fed-neutral point balancing algorithm. Simulation Modelling Practice and Theory. 29: 1-17.

[12] Belmokhtar K, Doumbia M. L and Agbossou K. 2014. Novel fuzzy logic based sensorless maximum power point tracking strategy for wind turbine systems driven DFIG (doubly-fed induction generator). Energy. 76, 679-693.

[13] Mohseni M, Islam S and Masoum M. A. 2011. Using equidistant vector-based hysteresis current regulators in DFIG wind generation systems. Electric Power Systems Research. 81(5): 1151-1160.

[14] Phan V. T, Logenthiran T, Woo W. L, Atkinson D and Pickert V. 2016. Analysis and compensation of voltage unbalance of a DFIG using predictive rotor current control. International Journal of Electrical Power & Energy Systems. 75, 8-18.

[15] Liao Y, Li H and Yao J. 2011. Unbalanced-grid-fault ride-through control for a doubly fed induction generator wind turbine with series grid-side converter. WSEAS Transactions on Circuits and Systems. 10(2): 69-82.

[16] Yousefi-Talouki A, Pouresmaeil E and Jorgensen B.N. 2014. Active and reactive power ripple minimization in direct power control of matrix converter-fed DFIG. International journal of electrical power and energy systems. 63: 600-608.

[17] Dionísio Barros J and Fernando Silva J. 2008. Optimal Predictive Control of Three-Phase NPC Multilevel Converter for Power Quality Applications. IEEE transactions on industrial electronics. 55(10).

[18] Francis A. O and Gauthier S. 2010. A Novel Robust Nonlinear Control of a Three-Phase NPC Inverter Based Active Power Filter. WeC05.2, American Control Conference, Marriott Waterfront, Baltimore, MD, USA.

[19] Abbes M, Belhadj J. 2012. New control method of a robust NPC converter for renewable energy sources grid connection.

[20] Barros J. D and Silva J. F. 2008. Optimal predictive control of three-phase NPC multilevel converter for power quality applications. Industrial Electronics, IEEE Transactions on. 55(10): 3670-3681.

[21] Watanabe E. H, Aredes M, Afonso J. L, Pinto J. G, Monteiro L. F. C and Akagi H. 2010. Instantaneous p–q power theory for control of compensators in micro-grids. In Nonsinusoidal Currents and Compensation (ISNCC), International School on (pp. 17-26).

[22] Yazdani A and Iravani R. 2005. A generalized state-space averaged model of the three-level NPC converter for systematic DC-voltage-balancer and current-controller design. Power Delivery, IEEE Transactions on. 20(2): 1105-1114.

[23] Barra A, Ouadi H, Giri F. 2016. Sensorless Nonlinear Control of Wind Energy Systems with Doubly Fed Induction Generator. Journal of control, Automation and Electrical Systems. 27(5): 562-578.

[24] Zhao Y, Wei C, Zhang Z, and Qiao W. 2013. A review on position/speed sensorless control for permanent magnet synchronous machine-based wind energy conversion systems. IEEE Journal of Emerging and Selected Topics in Power Electronics. I(4): 203-216.